CHEMISTRY OF MATERIALS
Article
Cite This: Chem. Mater. 2019, 31, 7910−7921
pubs.acs.org/cm

Downloaded via KING ABDULLAH UNIV SCI TECHLGY on February 9, 2022 at 10:55:43 (UTC).
See https://pubs.acs.org/sharingguidelines for options on how to legitimately share published articles.

Fluorinated Covalent Organic Polymers for High Performance Sulfur Cathodes in Lithium−Sulfur Batteries

Hyuksoo Shin,[†,§] Doyun Kim,[‡,§] Hyeon Jin Kim,[†,§] Jiheon Kim,[†] Kookheon Char,[*,†] Cafer T. Yavuz,[*,‡] and Jang Wook Choi[*,†]

[†]School of Chemical and Biological Engineering and Institute of Chemical Processes, Seoul National University, 1 Gwanak-ro, Gwanak-gu, Seoul 08826, Republic of Korea

[‡]Department of Chemical and Biomolecular Engineering, Korea Advanced Institute of Science and Technology (KAIST), 291 Daehak-ro, Yuseong-gu, Daejeon, 34141, Republic of Korea

Supporting Information

ABSTRACT: Lithium−sulfur (Li−S) batteries by far offer higher theoretical energy density than that of the commercial lithium-ion battery counterparts, but suffer predominantly from an irreversible shuttling process involving lithium polysulfides. Here, we report a fluorinated covalent organic polymer (F-COP) as a template for high performance sulfur cathodes in Li−S batteries. The fluorination allowed facile covalent attachment of sulfur to a porous polymer framework via nucleophilic aromatic substitution reaction (S$_N$Ar), leading to high sulfur content, e.g., over 70 wt %. The F-COP framework was microporous with 72% of pores within three well-defined pore sizes, viz. 0.58, 1.19, and 1.68 nm, which effectively suppressed polysulfide dissolution via steric and electrostatic hindrance. As a result of the structural features of the F-COP, the resulting sulfur electrode exhibited high electrochemical performance of 1287.7 mAh g^{-1} at 0.05C, 96.4% initial Columbic efficiency, 70.3% capacity retention after 1000 cycles at 0.5C, and robust operation for a sulfur loading of up to 4.1 mg$_{sulfur}$ cm^{-2}. Our findings suggest the F-COP family with the adaptability of S$_N$Ar chemistry and well-defined microporous structures as useful frameworks for highly sustainable sulfur electrodes in Li−S batteries.

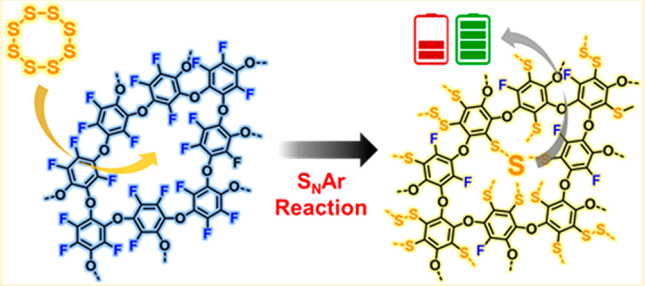

INTRODUCTION

High performance rechargeable lithium-ion batteries (LIBs), in recent years, are in increasing demand mainly because of the need to power advanced portable electronic devices and green electrified transportations.[1,2] The aim to operate these applications without frequent charging is the primary driving force of the major research and development efforts, and to this end, the lithium−sulfur (Li−S) batteries offer high energy densities that could satisfy such technological demand.[3−7]

Discharge process in Li−S batteries is based on the redox reaction between elemental sulfur and Li ions, which sequentially produces long-chain and short-chain lithium polysulfides (LiPSs). The low molecular weight of elemental sulfur, together with high Li-to-S ratios, enables the theoretical energy density of a Li−S cell to reach 2600 Wh kg^{-1}, which is approximately 7 times larger than the classical LIBs (~387 Wh kg^{-1}). Typically, a large amount of elemental sulfur is produced as a surplus from petroleum refining process; therefore, this sulfur can be readily used as a cheap raw material.[8−10] In spite of these clear advantages, commercialization of Li−S batteries has been slow due to certain longstanding technical challenges, such as poor electrical conductivity of elemental sulfur (~10^{-30} S cm^{-1}), shuttling of soluble long-chain LiPS species in liquid electrolytes, and large volume change (~80%) of active material during repetitive charge−discharge cycling.[11,12]

Physical and chemical encapsulation of elemental sulfur in various porous hosts is a viable approach to overcome the drawbacks of the Li−S batteries. In the physical confinement strategy, diverse porous carbon frameworks, including mesoporous carbons,[13−15] graphene,[16−18] graphene oxide,[19−21] carbon spheres,[22,23] and carbon nanotubes,[24−26] demonstrated decent electrochemical performance. This is because the carbonaceous materials can supplement the low electrical conductivity of elemental sulfur, while the confined sulfur can largely avoid LiPS dissolution. Other materials, such as conducting polymers,[27−29] metal−organic frameworks (MOFs),[30−35] covalent organic frameworks (COFs),[36−40] and porous organic polymers (POPs),[41−47] were also introduced as sulfur hosts in a similar context. Despite the improved cycling performance, complete termination of the LiPS shuttling is not still fully warranted due to the limited binding affinity between the physisorptive hosts and LiPSs.

Received: May 21, 2019
Revised: September 9, 2019
Published: September 11, 2019

ACS Publications © 2019 American Chemical Society

DOI: 10.1021/acs.chemmater.9b01986

In an alternative direction, elemental sulfur can be covalently (thus chemically) linked to organic/polymer frameworks. For example, arylethenyl monomer was reacted with molten sulfur via the so-called inverse vulcanization,[48] resulting in linear sulfur chains dispersed in organic domains. Through the inverse vulcanization approach, high sulfur content above 90 wt % was achieved along with decent cycling performance. Trithiocyanuric acid was also used to have ring opening polymerization of elemental sulfur via radical reaction of Ar-SH moieties with polysulfide diradical. This approach resulted in a sulfur content of 63 wt % by providing anchoring sites to elemental sulfur.[49] In addition, nucleophilic aromatic substitution reaction (S_NAr) between perfluoroaryl units and elemental sulfur was introduced for a high yield sulfur substitution,[50] which was beneficial in increasing the sulfur content in the polymeric framework. Since S_NAr is a convenient yet versatile strategy applicable to electron-deficient aromatic compounds, a wide range of polymers containing similar aromatic components can be used as sulfur cathode materials.

In the current study, we employed S_NAr for polysulfide stabilization in ultramicroporous POPs. Recently, Luo et al. identified[51] that the minimal pore size for penetration of Li_2S_4 is 1.18 nm (on neutral surfaces). The fine-tuning of the pore size in POP structures with confinement under 1 nm should be able to provide the necessary cutoff to block LiPS dissolution. We, therefore, selected a member from the covalent organic polymer (COP) family, viz. COP-99, as the porous polymeric host which comes with high loading of aromatic fluorines. Prior research reported[52] that COP-99 can separate water-soluble organic molecules depending on their charges and sizes, proving its well-controlled pore dimensions and charge polarization ability. However, the aromatic fluorines in COP-99 readily allow covalent attachment of sulfur via S_NAr. Taking advantage of the well-defined sulfur attachment and the inherent porosity of COP-99, its sulfurized form (denoted as S-COP-99) exhibited decent electrochemical performance as a sulfur cathode: specific capacity of 1287.7 mAh g^{-1} at 0.05C, 96.4% initial Columbic efficiency (ICE), 70.3% capacity retention at 0.5C after 1000 cycles, and robust operation at a sulfur loading of up to 4.1 mg_{sulfur} cm^{-2}.

EXPERIMENTAL SECTION

Materials. Tetrafluorohydroquinone (TFHQ) was purchased from TCI, Japan. Anhydrous cesium carbonate (CS_2 CO^3) was purchased form SAMCHUN, South Korea. Elemental sulfur, anhydrous N,N-dimethylformamide (DMF), polyvinylidene fluoride (PVDF, M_w = 560 000), lithium bis(trifluoromethane)sulfonimide (LiTFSI), lithium nitrate ($LiNO_3$), dimethyl ether (DME), and 1,3-dioxolane (DOL) were purchased from Sigma-Aldrich, U.S.A. *N*-Methyl-2-pyrrolidone (NMP) was purchased from Junsei Chemical, Japan. All materials were used without further purification.

Synthesis of COP-99. A new COP-99 was produced by a slightly modified synthetic procedure.[52] TFHQ (1.0 g, 5.49 mmol) was dissolved in dry DMF (25 mL) and heated at 80 °C in Ar atmosphere. Then, instead of treating the solution with K_2CO_3, we used Cs_2CO_3 (1.2 g, 3.68 mmol) under inert conditions and the mixture was heated at 145 °C in Ar atmosphere for 24 h. After cooling to room temperature, water was added to the reaction mixture which yielded a dark brown precipitate. The precipitate was filtered and rinsed with water and acetone until the filtrate became clear. The obtained powder was dried under vacuum at 130 °C overnight. COP-99 (0.68 g, 79% yield) was obtained as a dark brown powder and characterized further. Anal. for original COP-99: C, 50.05; H, 0.87; O, 26.73; F, 21.51; N, 0.92; Found: C, 49.59; H, 1.27; O, 25.91; F, 18.30; N, 1.26. S_{BET} (Ar adsorption, 87 K) = 545.9 m^2 g^{-1}.

Synthesis of S-COP-99s. COP-99 (0.1 g) and elemental sulfur were introduced in a pyrex ampule in Ar atmosphere at different weight ratios from 1:3 to 1:5. The ampule was then evacuated, flame-sealed and heated in a box furnace. The temperature of the box furnace was slowly increased to 160 °C for 2 h and was maintained at this temperature for 15 h. The temperature was subsequently increased further to the reaction temperatures (i.e., 200, 300, 400, and 450 °C) in the next 2.5 h and was maintained for 15 h. After cooling down to room temperature, S-COP-99s were obtained as brownish-black powder in quantitative yield.

Electrochemical Characterization of S-COP-99s. The electrochemical properties of S-COP-99s were evaluated by fabricating CR2032-type coin cells. The sulfur electrodes were prepared by dispersing S-COP-99s with conductive agent (carbon black/CNT) and PVDF in NMP in the mass ratio 7:2:1. The as-prepared slurries were cast onto aluminum foil (20 μm, Hohsen, Japan) using the doctor-blade technique. The electrodes were then dried in a convection oven at 60 °C overnight. The coin cells were assembled in an Ar-filled glovebox with Li metal discs paired as both counter and reference electrodes. Polypropylene membrane (Celgard 2400) was used as separator, and a solvent mixture of DOL/DME in 1:1 (v/v) containing LiTFSI (1.0 M) and $LiNO_3$(0.2 M) was used as the electrolyte. The relative electrolyte amount to the sulfur amount was fixed at 14 mL g_{sulfur}^{-1} for all evaluations. All electrochemical characterizations were carried out using a WBCS 3000 battery cycler (Wonatech, South Korea) and VSP (Bio-Logic, France). Galvanostatic measurements were conducted in the voltage range 1.7−2.7 V versus Li/Li^+, and electrochemical impedance spectroscopy (EIS) analyses were carried out in the frequency range 1 MHz−0.01 Hz with amplitude of 10 mV at open-circuit voltage potential. Galvanostatic intermittent titration technique (GITT) measurements were conducted at a current density of 33.5 mA g^{-1} (0.02C). Each 1 h-scan was followed by a 2 h-rest step. Cyclic voltammetry (CV) measurements were performed at scan rates from 0.05 to 0.5 mV s^{-1}. The current densities and specific capacities from all the evaluations were calculated based on the weight of sulfur only.

Physicochemical Characterization. ^{19}F magic-angle spinning solid nuclear magnetic resonance (NMR) spectra were recorded on a 400 MHz 54 mm NMR system (Agilent, South Korea). Porosity was analyzed with a 3-flex (Micromeritics, U.S.A.) using argon gas as the probe gas at 87 K. COP-99 was degassed at 130 °C under vacuum overnight. The specific surface area was calculated based on Brunauer−Emmett−Teller (BET) model, and the pore size distribution was determined by nonlocal density functional theory (NLDFT) method. Fourier-transform infrared spectroscopy (FT-IR) analysis was conducted with Nicolet iS50, a Scientific Instrument (Thermo Fisher, Germany). Elemental analysis (EA) was performed by an elemental analyzer (Flash 2000 series (CHNSO), studies were done using DSC 4000 (PerkinElmer, U.S.A.) at a heating and cooling rate of 10 °C min^{-1}. Raman spectra were obtained from a LabRAM HV Evolution (Horiba, Japan) spectrometer. Field-emission scanning electron microscopy (FE-SEM) images were obtained using a JSM-7600F (JEOL, Japan).

Thermo Fisher, Germany) and an X-ray fluorescence (XRF) spectrometer (ZSX Primus II, Rigaku, Japan). The elemental contents of C, H, O, and S were obtained from the EA, and the C-to-F ratio was obtained from XRF studies. Thermogravimetric analysis (TGA) was carried out using TGA Q500 (TA Instruments, U.S.A.) at a heating rate of 10 °C min^{-1} up to 600 °C in nitrogen atmosphere. X-ray photoelectron spectroscopy (XPS) spectra were recorded on an AXIS-His (KRATOS, U.K.) spectrometer. Differential scanning calorimeter (DSC).

RESULTS AND DISCUSSION

In order to construct a microporous, highly fluorinated, sustainable, covalently linked, porous network, we turned to aromatic ether formation reactions through the coupling

DOI: 10.1021/acs.chemmater.9b01986
Chem. Mater. 2019, 31, 7910−7921

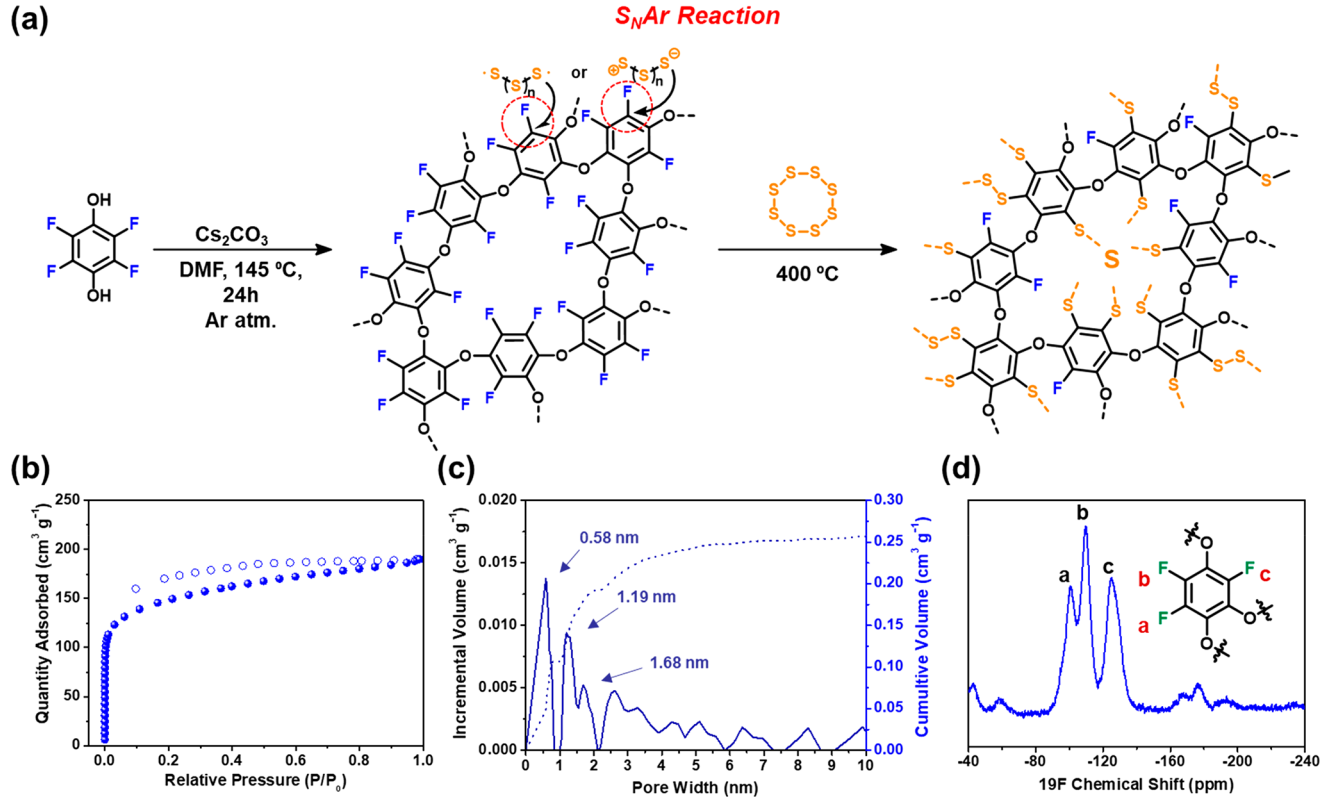

Figure 1. (a) Synthesis of S-COP-99 series from a commercial building block and subsequent covalent attachment of elemental sulfur through substitutional chemistry within the microporous superstructure. (b) Argon adsorption−desorption isotherms of COP-99, (c) the corresponding NLDFT pore size distribution. (d) Solid-state ^{19}F-NMR spectrum of COP-99.

Table 1. Elemental Weight Compositions of COP-99 and S-COP-99s Obtained from EA and XRF

samples	nitrogen (wt %)	carbon (wt %)	hydrogen (wt %)	sulfur (wt %)	oxygen (wt %)	fluorine (wt %)	total (wt %)
COP-99	1.3	49.6	1.3	n.d.	25.9	18.3	96.4
S-COP-99 (1:3)	0.5	14.5	0.2	74.1	7.7	4.6	101.6
S-COP-99 (1:4)	0.4	11.4	0.1	79.0	6.1	5.1	102.1
S-COP-99 (1:5)	0.3	8.8	0.1	81.4	4.6	5.6	100.8

chemistry of deprotonated phenols with perfluorinated substrates via S_NAr mechanism.[53] Following a slightly modified procedure[52] (see Experimental Section for details on methods), the COP-99 was, therefore, synthesized from a one-pot self-polymerization of widely available tetrafluorohydroquinone with common alkali carbonates (Figure 1a). The Cs_2CO_3 yielded optimal porosity with the highest pore volume.[52] The porosity of COP-99 was investigated using argon gas probe at 87 K since fluorine is known to interact with N_2 and might lead to erroneous results.[54] The COP-99 showed type I isotherm with pore volume contributed primarily by micropores (72%), thereby indicating a predominantly microporous structure. The BET specific surface area was calculated to be 546 m^2 g^{-1} and the pore volume was 0.268 cm^3 g^{-1} (Figure 1b). The pore size distribution was estimated using a NLDFT with infinite slit pore approximation (Supporting Information, SI, Figure S1).[55,56] COP-99 was found to feature three major pore sizes, viz. 0.58, 1.19, and 1.68 nm, i.e., all below 2 nm, therefore, confirming microporosity (Figure 1c). The measured fluorine content was 18.3 wt % (Table 1). FT-IR spectrum showed a set of peaks, viz. 1050 cm^{-1}, 1296 cm^{-1}, and 1450 cm^{-1}, which corresponded to the C−F stretching, C−O−C stretching, and C═C stretching, respectively (SI Figure S2). The ^{19}F solid NMR spectrum of COP-99 confirmed the superstructure and the asymmetric distribution of aromatic fluorides at precisely −100.7 ppm, −109.6 ppm, and −125.0 ppm (Figure 1d). S-COP-99 analogues were then synthesized by simply reacting elemental sulfur with COP-99 at different reaction temperatures, viz. 200, 300, 400, and 450 °C, to identify a suitable synthetic condition for the S_NAr reaction between linear ionic sulfur species and COP-99. Once the reactions were complete, the amount of the residual fluorine was assessed by XRF spectroscopy (Table 2). The carbon-to-fluorine ratio was found to decrease gradually from 100:47 to 100:24 with increasing reaction temperature from 200 to 450 °C. This indicated an increased substitution of

Table 2. XRF Analysis of S-COP-99s Synthesized at Various Temperatures

samples	carbon/fluorine (mol/mol)
S-COP-99−200 °C	100:47
S-COP-99−300 °C	100:35
S-COP-99−400 °C	100:28
S-COP-99−450 °C	100:24

DOI: 10.1021/acs.chemmater.9b01986
Chem. Mater. 2019, 31, 7910−7921

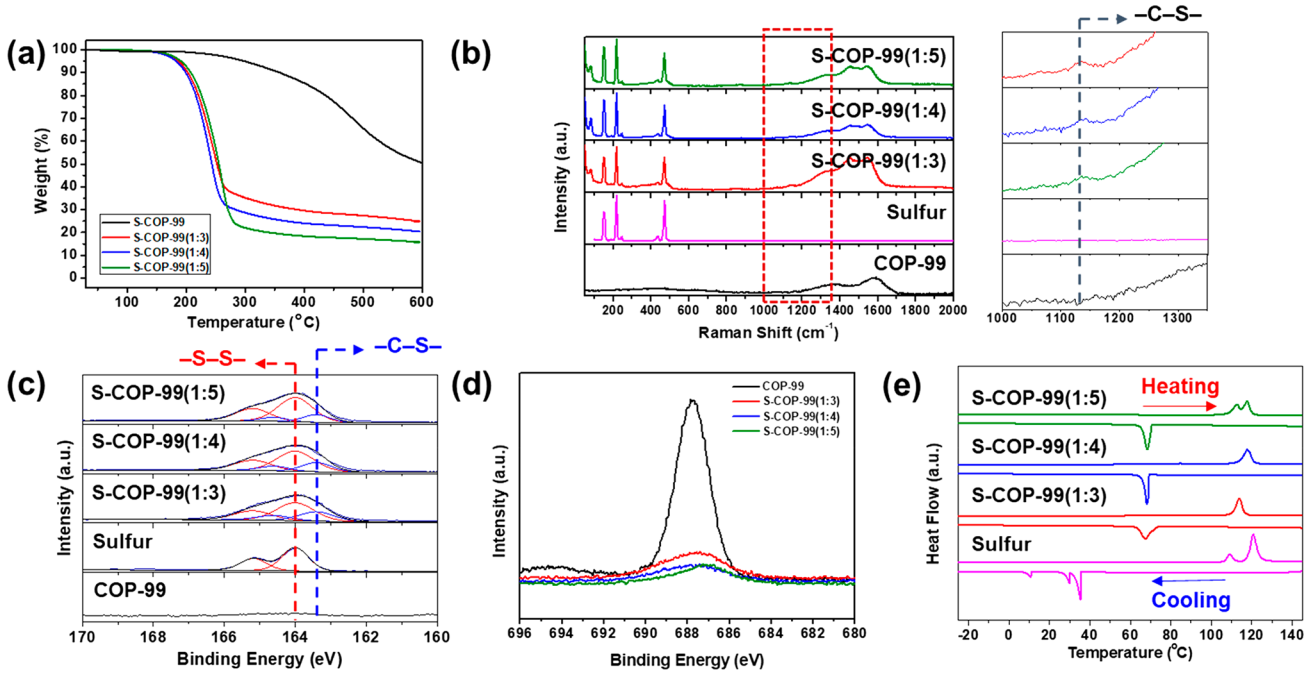

Figure 2. Structural analysis of COP-99 and S-COP-99s with different sulfur loadings. (a) TGA curves of COP-99 and S-COP99s in N_2 atmosphere. (b) Raman spectra of elemental sulfur, COP-99, and S-COP-99s. (c) S 2p XPS spectra and (d) F 1s XPS spectra of COP-99 and S-COP-99s. (e) DSC profiles of elemental sulfur and S-COP-99s.

fluorine by sulfur with increase in the reaction temperature. Another feature to consider carefully was the existence of a critical temperature beyond which the COP-99 framework thermally degrades. In an attempt to determine the sulfur content and thermal stability,

TGA of COP-99 and S-COP-99s were conducted in N_2 atmosphere (SI Figure S3). On the basis of the weight loss in the temperature range of 200−300 °C, S-COP-99 analogues synthesized at 200, 300, 400, and 450 °C had 72.2, 71.0, 71.3, and 59.4 wt % left over masses, respectively. Remarkably, S-COP-99−200 °C and S-COP-99−300 °C exhibited distinct mass loss above 350 °C, suggesting the decomposition of the residual C−F bonds. This observation can be rationalized using bond dissociation energies; the dissociation energy of C−F bond (450 kJ mol^{-1}) is higher than those of C−S and S−S bonds (260 and 225 kJ mol^{-1}, respectively).[57,58] However, the lower sulfur content of S-COP-99−450 °C could be ascribed to the disintegration of the COP-99 framework, where sulfur could not be contained properly. Since S-COP-99−400 °C showed a stable TGA profile throughout the operational temperature range, 400 °C was adopted as the optimal temperature. The identification of the optimal reaction temperature was further verified by evaluating the electrochemical performance of the S-COP-99 series. For this purpose, the S-COP-99 derivatives were subjected to cycling tests at 0.5*C* (1*C* = 1675 mA g^{-1}) with an areal sulfur loading of 1.0 mg_{sulfur} cm^{-2} (SI Figure S4). The S-COP-99−200/300/400/450 °C electrodes showed initial capacities of 798.6, 741.1, 762.0, and 999.9 mAh g^{-1}, respectively. After 300 cycles, these capacities decayed to 526.7, 502.3, 617.8, and 454.9 mAh g^{-1}, respectively, corresponding to 66.0%, 67.8%, 81.1%, and 45.5% capacity retentions with respect to their initial capacities. The severe capacity decay of S-COP-99−450 °C could be related to the aforementioned collapse of the polymer framework. On a related note, the higher capacity retention of S-COP-99−400 °C can be attributed to the covalent attachment of the sulfur to the stable polymer framework.

Furthermore, different COP-99-to-sulfur weight ratios of 1:3, 1:4, and 1:5 were tested keeping the reaction temperature fixed at 400 °C. The new S-COP-99s exhibited typical curves of the sulfur-polymer composites in their TGA profiles where rapid decline around 200 °C was observed which represented the decomposition of sulfur (Figure 2a). According to the weight loss in the temperature range 200−300 °C, the sulfur contents of S-COP-99(1:3), S-COP-99(1:4), and S-COP-99(1:5) were calculated as 64.7, 71.3, and 77.8 wt %, respectively, which were also largely consistent with the EA results (Table 1). The bonding nature of sulfur in the S-COP-99s was investigated by dispersive Raman spectroscopy (Figure 2b). While the peaks located at 151, 216, and 470 cm^{-1} were attributed to the S−S stretching mode, the peak at 1117 cm^{-1} was related to the C−S stretching mode.[59−62] To further elucidate the detailed bonding nature of S-COP-99s, XPS was carried out in the binding energy ranges corresponding to S 2p, C 1s, and F 1s levels. The S 2p spectra of S-COP-99s exhibited S−S and C−S bonds at 164.0 and 163.4 eV, respectively (Figure 2c). The emergence of new peak at 163.4 eV, which is absent with elemental sulfur and COP-99, clearly verified the formation of the C−S bond. The C 1s spectra of COP-99 and S-COP-99s exhibited three peaks at 284.8, 286.0, and 287.2 eV, which were assigned to the carbon atoms of phenyl moiety, specifically the C−C, C−S and C−O, and C−F bonds, respectively (SI Figure S5).

To note, the intensity of the phenyl peak was preserved with increasing weight ratio of sulfur from COP-99 to S-COP-99(1:5), but the intensity of the C−F peak decreased gradually and eventually disappeared for S-COP-99(1:4) and (1:5). This decrease of the C−F peak intensity was in good agreement with the decreased peak at 687.8 eV in the F 1s branch (Figure 2d), reconfirming a facile F-to-S substitution through the S_NAr chemistry. The intensity of the F 1s peak ultimately became

DOI: 10.1021/acs.chemmater.9b01986
Chem. Mater. 2019, 31, 7910−7921

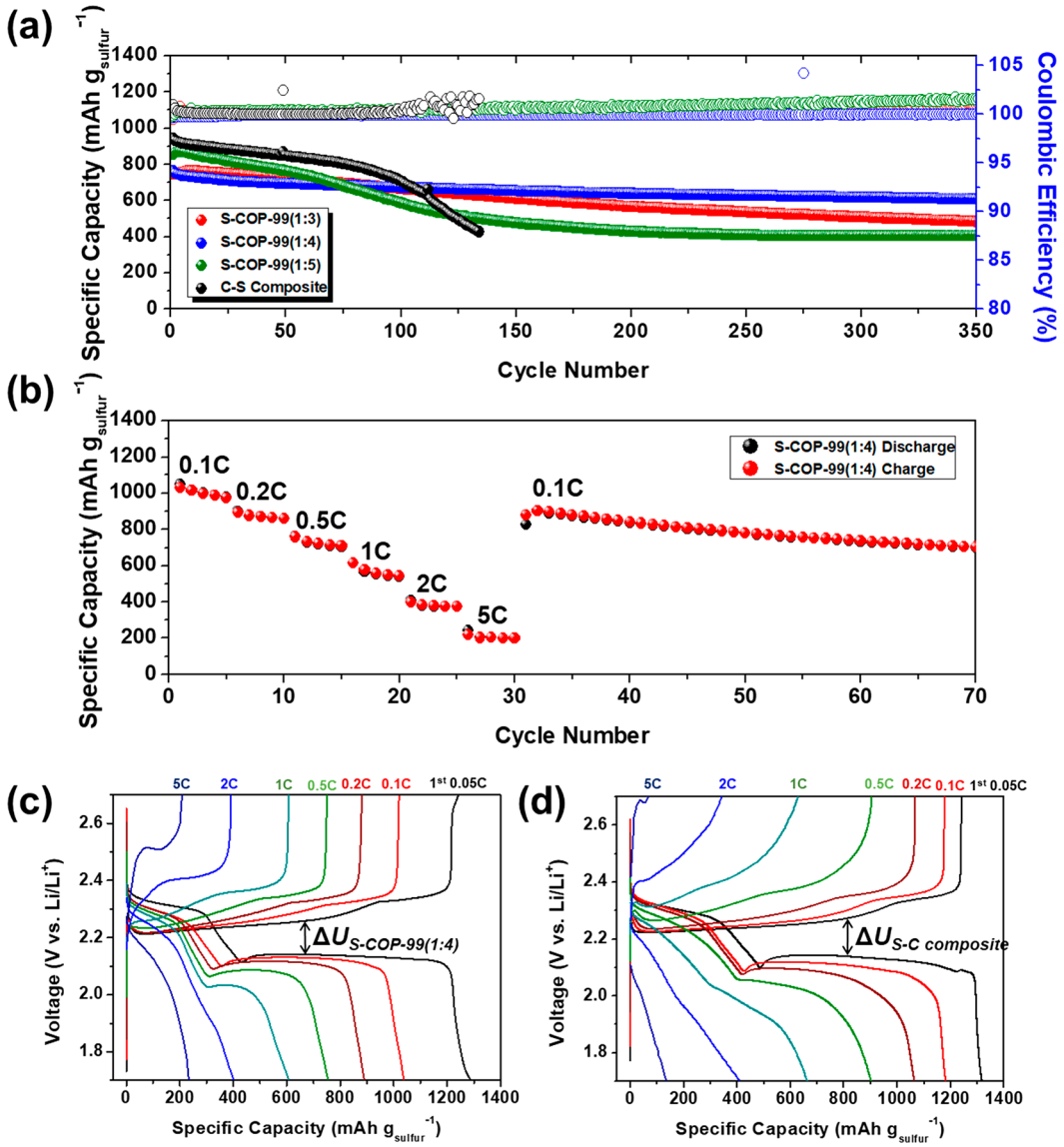

Figure 3. (a) Cycling performance of S-COP-99(1:3), S-COP-99(1:4), S-COP-99(1:5), and C−S composite with sulfur loading of 1.0 mg_{sulfur} cm^{-2} at 0.5*C*. (b) Rate performance of S-COP-99(1:4) evaluated at various *C*-rates in the voltage range 1.7−2.7 V. Discharge−charge curves of (c) S-COP-99(1:4) and (d) C−S composite evaluated at various *C*-rates in the voltage range 1.7−2.7 V.

saturated in S-COP-99(1:4) and the weight ratios above 1:4 showed no further effect on the F-to-S substitution. According to the DSC analyses (Figure 2e), the elemental sulfur exhibited typical phase transition from orthorhombic α-sulfur to monoclinic β-sulfur.

The DSC profile of elemental sulfur also revealed melting transition[63] of β-sulfur during the heating scan as well as crystallization of α-sulfur and β-sulfur during the cooling scan. However, the DSC spectra of S-COP-99(1:3) and S-COP-99(1:4) exhibited one melting transition during the heating scan and the peaks related to crystallization were up-shifted during the cooling scan. These observations implied that the sulfur in S-COP-99s lost the cyclic configuration of S_8, and its chains shortened[64] due to the covalent attachment to the microporous polymer. By contrast, S-COP-99(1:5) still exhibited an α-to-β phase transition peak during the heating scan, which was attributed to overimpregnation of sulfur.

The effect of different amounts of sulfur substitution was corroborated focusing on the electrode film morphology by performing FE-SEM analysis (SI Figure S6). While the SEM image of pristine COP-99 exhibited monodisperse particulate morphology, the particle boundaries became unclear for S-COP-99(1:3) and S-COP-99(1:4) after sulfur impregnation. However, sulfur began to aggregate in S-COP-99(1:5), a signature of the overimpregnation of sulfur. In an attempt to identify an optimal sulfur ratio in S-COP-99s, cycling performance of S-COP-99(1:3), (1:4), and (1:5) was evaluated at 0.5*C* (1C = 1675 mA g^{-1}) with an areal sulfur loading of 1.0 mg_{sulfur} cm^{-2} (Figure 3a). A control sample, denoted as C−S composite, was prepared in parallel by simple physical mixing of elemental sulfur and commercial activated carbon (YP-50F) in a mass ratio of 70:30, followed by thermal annealing at 155 °C. At this *C*-rate, the S-COP-99 electrodes exhibited initial discharge capacities of 743.5, 762.0, and 853.2 mAh g^{-1}, respectively, along with capacity retentions of 65.0%, 79.9%, and 47.7% after 350 cycles. The initial specific capacities followed the same trend as the sulfur content (Table 1). Despite the highest sulfur content and consequent

DOI: 10.1021/acs.chemmater.9b01986
Chem. Mater. 2019, 31, 7910−7921

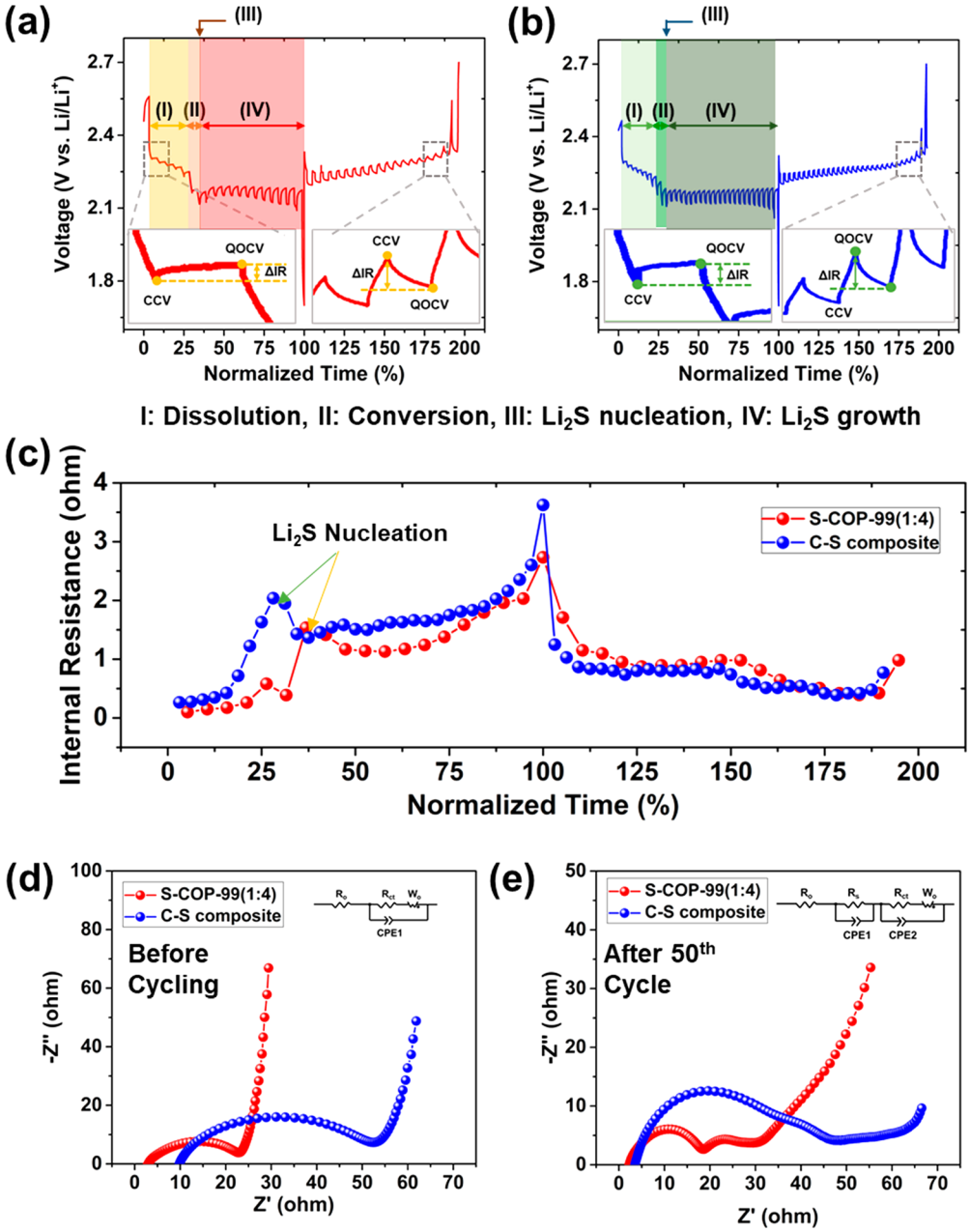

Figure 4. GITT plots of (a) S-COP-99(1:4) and (b) C−S composite. (c) Internal resistances of S-COP-99(1:4) and C−S composite with respect to normalized discharge−charge time. Nyquist plots of S-COP-99(1:4) and C−S composite cells (d) before cycling and (e) after 50 cycles. Insets: equivalent circuits for fitting of Nyquist plots.

specific capacity, S-COP-99(1:5) suffered from inferior cycling performance compared to that of the other two counterparts. This poor cycling performance can be explained by the over-impregnation of sulfur (as indicated in SI Figure S6d) that accelerated polysulfide dissolution upon the reaction with Li ions. Although elemental sulfur should sublime at the reaction temperature of 400 °C, the reaction was performed in a closed ampule so that residual sulfur could exist upon cooling down to room temperature as in the case of S-COP-99(1:5). On the basis of the series of electrochemical evaluation, it was concluded that S-COP-99(1:4) offers the most promising properties, and thus further electrochemical analyses were done only with this sample.

When measured at 0.05*C*, the S-COP-99(1:4) showed discharge and charge capacities of 1287.8 and 1241.5 mAh g^{-1}, respectively, in its first cycle, leading to an initial Coulombic efficiency (ICE) of 96.4% ($C_{charge}/C_{discharge}$). This ICE value is quite noticeable, as some sulfurized polymers, such as sulfur-polyacrylonitrile (S-PAN), are liable to Li trapping in the first cycle, resulting in poor ICEs even below 80%.[65−67] When subjected to various *C*-rates, the S-COP-99(1:4) displayed decent performance in regard to capacity loss. When the *C*-rate increased from 0.05*C* to 0.1*C*, 0.2*C*, 0.5*C*, 1*C*, 2*C*, and 5*C*, its discharge capacity changed from 1287.8 mAh g^{-1} to 1050.2, 900.2, 762.9, 615.1, 406.9, and 243.1 mAh g^{-1}, respectively, corresponding to capacity retention of 81.5%, 69.9%, 59.2%, 47.8%, 31.6, and 18.9% with respect to the capacity at 0.05*C* (Figure 3b). Upon returning to 0.1*C*, 902.5 mAh g^{-1} was recovered, corresponding to 92.4% retention with respect to the fifth cycle at the same *C*-rate.

DOI: 10.1021/acs.chemmater.9b01986
Chem. Mater. 2019, 31, 7910−7921

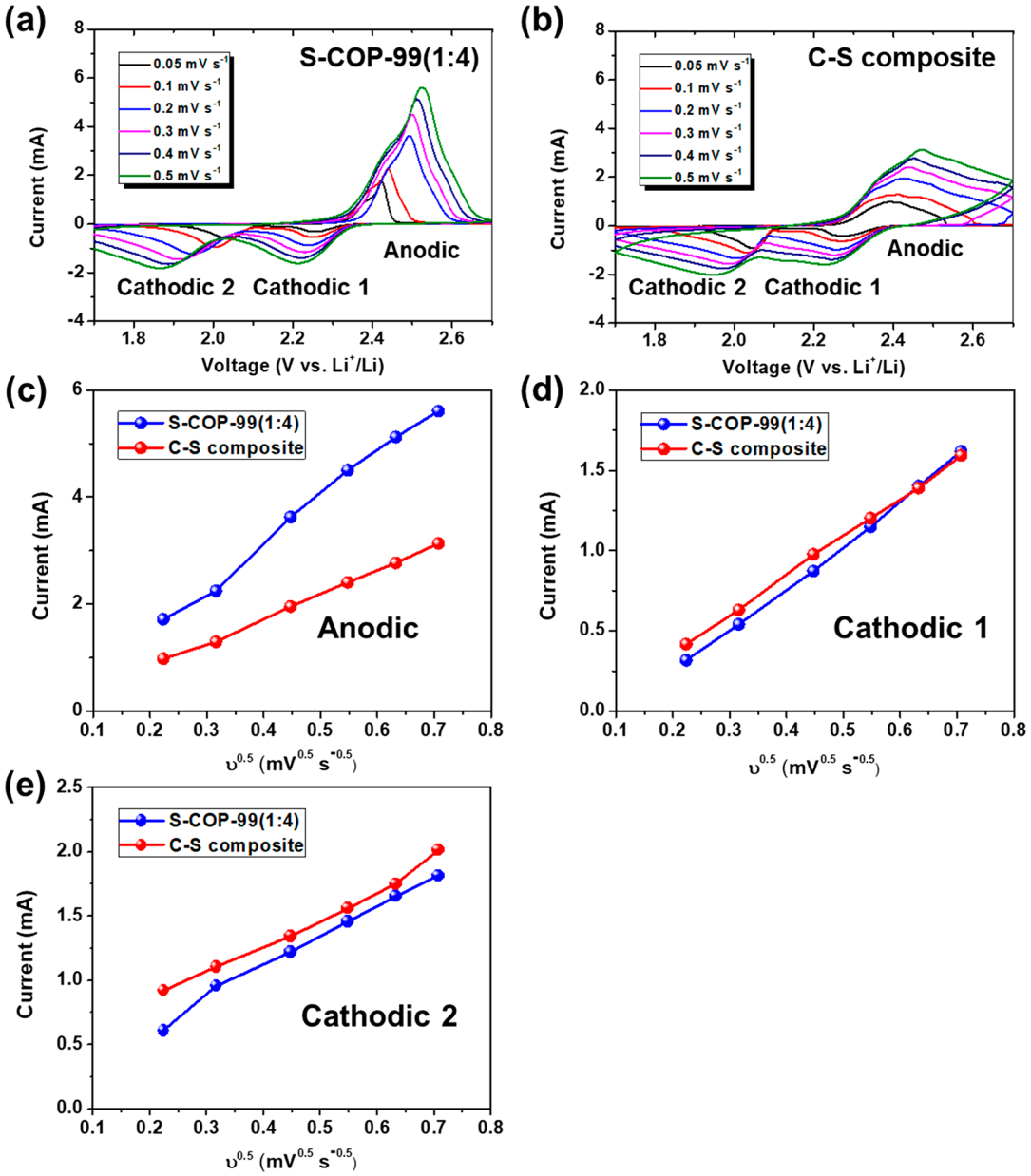

Figure 5. CV plots of (a) S-COP-99(1:4) and (b) C−S composite in the potential range 1.7−2.7 V at various scan rates. Plots of CV peak current vs the square root of scan rate for (c) the anodic reaction, (d) the cathodic reaction 1 ($S_8 \rightarrow Li_2S_4$), and (e) the cathodic reaction 2 ($Li_2S_4 \rightarrow Li_2S$). Each anodic and cathodic reaction is denoted in (a) and (b).

The substantial capacities observed at high *C*-rates was indicative of kinetically efficient (de)lithiation process with S-COP-99(1:4), which also suggested that insulating sulfur was well-distributed across the COP-99 framework forming nanodomains while the nanopores effectively suppressed the LiPS shuttling via size restriction. Interestingly, the voltage profiles appeared different depending upon the *C*-rate (Figure 3c); at lower *C*-rates, e.g., 0.1*C*−1*C*, the discharging profiles exhibited two distinct plateaus at around 2.4 and 2.1 V. By contrast, at 2*C* and 5*C*, the lower plateaus could be hardly observed due to slow kinetics[68,69] of the liquid-to-solid conversion reaction at the lower plateau regime. The reaction at the lower plateau involved $Li_2S_4(l)$-to-$Li_2S(s)$ conversion which was initiated by the nucleation of Li_2S.[70] However, the lower plateau of the C−S composite began to disappear at 1*C*, and the voltage differences between its charge and discharge plateaus (ΔU) were higher compared to those of the S-COP-99(1:4) at all *C*-rates (Figure 3d). The increase of C−S composite in the activation overpotential along the low plateau regime can be explained by the accelerated nucleation of Li_2S through the larger Li_2S_4 domains which made the subsequent Li_2S growth difficult due to limited electron transport in the corresponding domains.

In order to further elucidate the reaction kinetics of S-COP-99(1:4), GITT measurements were conducted at 0.02*C* rate (Figure 4). In the dissolution and conversion regimes (region I and II in the upper plateau), the S-COP-99(1:4) electrode (Figure 4a) clearly exhibited lower polarization in its discharging profile compared to that of the C−S composite (Figure 4b). For reference, in the time-normalized plot, the combined dissolution and conversion regimes occupy 25% and the Li_2S nucleation and growth regimes occupy the remaining

DOI: 10.1021/acs.chemmater.9b01986
Chem. Mater. 2019, 31, 7910−7921

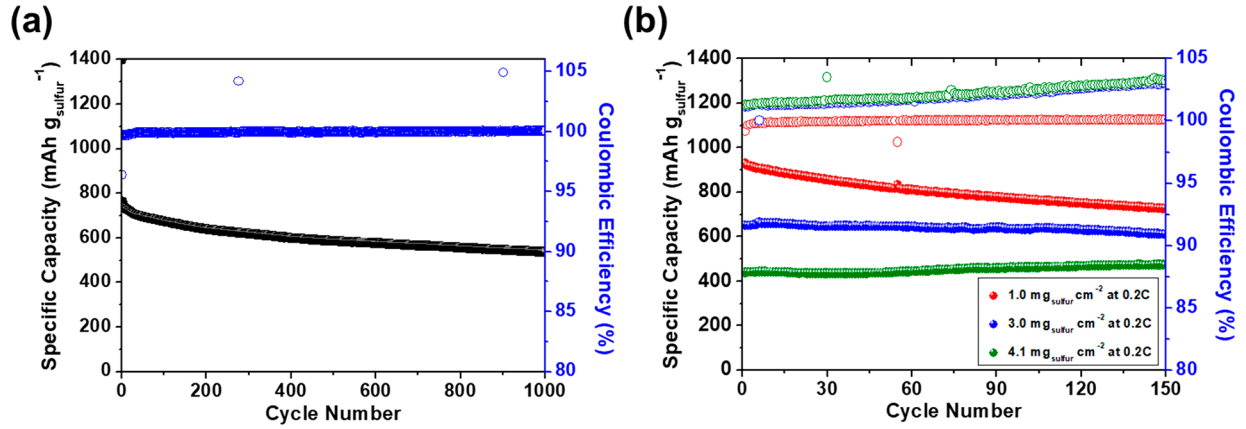

Figure 6. (a) Cycling performance and Coulombic efficiencies of S-COP-99(1:4) evaluated at 0.5C. (b) Capacity retentions of S-COP-99 (1:4) with various sulfur loadings when measured at 0.2C (1C = 1675 mA g^{-1}).

75%.[71] The substantially lower polarization in the upper plateau regime indicated superior dissolution kinetics of S-COP-99(1:4) which originated from its smaller sulfur domains. The polarization during electrochemical operation was quantified by introducing internal resistance, based on the following equation:[72,73]

$$\Delta R_{int}(\Omega) = |\Delta V_{QOCV\text{-}CCV}|/I_{applied} \quad (1)$$

where ΔV is the voltage difference between the points of quasi-open circuit voltage and closed-circuit voltage, and $I_{applied}$ is the applied current. ΔR_{int} is plotted with respect to normalized time (Figure 4c). It is noteworthy that ΔR_{int} is noticeably higher in the Li_2S nucleation regime than that in the dissolution and conversion regimes (region I and II in the upper plateau), indicating that increase in the activation overpotential in the low plateau represents a higher energy barrier for the nucleation of Li_2S.[74,75] Thus, the smaller ΔR_{int} of S-COP-99(1:4) than that of the C−S composite reflected an enhanced nucleation kinetics of Li_2S[76] due to its confined distribution of sulfur. To further evaluate the electrochemical reaction kinetics, both the electrodes were subjected to EIS measurements (Figure 4d,e). It was observed that the Nyquist plots of both electrodes before cycling comprised a semicircle at the high and medium frequency regime and an inclined line at the low frequency regime. The high frequency intercept on the real axis was ascribed[77] to the bulk resistance (R_o) of the cell, which comprised the electrolyte and electrode resistances. The semicircle at the high-to-medium frequency regime can be attributed[78] to the interface charge-transfer resistance (R_{ct}), whereas the inclined line at the low-frequency regime to the Li-ion diffusion in the cathode, constituting the so-called Warburg impedance (W_o). Before cycling, the S-COP-99(1:4) electrode exhibited a relatively smaller R_{ct} (21.3 Ω) than that of the C−S composite electrode (45.0 Ω) due to a homogeneous distribution of sulfur in the COP framework in the former.

After 50 cycles, the semicircles in both the cells were split into two smaller circles. In these smaller circles, the semicircle in the high frequency regime corresponded to the surface resistance (R_s) reflecting irreversible deposition and aggregation of Li_2S_2/Li_2S layer on the surface of the cathode,[79] whereas the semicircle in the middle frequency regime corresponded to charge transfer process at the conductive agent interface.[80−85] After 50 cycles, the S-COP-99(1:4) still showed a relatively smaller R_s (14.7 Ω) and R_{ct} (11.7 Ω) than those of the C−S composite (27.9 and 22.6 Ω, respectively). In relation to the aforementioned rationale, the uniform distribution of sulfur in S-COP-99(1:4) along with suppressed formation of irreversible Li_2S layer resulted in a lower charge transfer resistance. The reproducibility of the results in Figures 3 and 4 was confirmed by testing five and three identical cells, respectively. In order to assess the lithium diffusion properties which was associated with LiPS dissolution, CV measurements were performed on both the electrodes at various scan rates ranging from 0.05 to 0.5 mV s^{-1} (Figure 5a,b). For both the electrodes, the cathodic and anodic peak currents were linear with the square root of the scan rate following the Randles-Sevcik equation:[86]

$$I_p = (2.69 \times 10^5)n^{1.5}aD^{0.5}v^{0.5}\Delta C_o \quad (2)$$

where I_p is the peak current, n is the number of electrons per reaction species, a is the active electrode area, D is the diffusion coefficient of Li ion, ΔC_o is the concentration change of Li ion upon the electrochemical reaction. Since n, a, and ΔC_o are constants in the battery system, from this relation, the linear fitting of peak current I_p versus $v^{0.5}$ yielded square root of Li-ion diffusion coefficients ($D^{0.5}$) as a factor in the slopes in Figure 5c−e. Interestingly, the slopes were clearly distinct for both electrodes with respect to anodic reaction (Figure 5c), whereas the difference became almost negligible for the cathodic reaction. The smaller slope of the C−S composite during the anodic reaction indicated its lower diffusivity than that of S-COP-99(1:4) during charging, and was thus ascribed to abundant high viscosity LiPSs dissolved in the electrolyte.[87,88] The superior diffusivity of S-COP-99(1:4) can be explained by suppressed LiPSs dissolution in the electrolyte that facilitated the diffusion of the electrolyte containing Li^+ ions. This also followed a similar trend as the low polarization in the dissolution and conversion regimes during GITT measurement.

The cyclability test was extended to see the sustainability of S-COP-99(1:4) for prolonged cycles (Figure 6a). When tested at 0.5C for 1000 cycles, remarkably, a discharge capacity of 535.9 mAh g^{-1} was retained, which corresponded to a capacity retention of 70.3%. This retention was translated to 0.03% capacity fading per cycle on average. Also, the average Coulombic efficiency throughout the cycling was 99.96%. Once again, these results reflected the sustainable structure of S-COP-99(1:4) in relation to the limited pore sizes and the heteroatoms that can afford to capture LiPSs.

DOI: 10.1021/acs.chemmater.9b01986
Chem. Mater. 2019, 31, 7910−7921

The S-COP-99(1:4) was additionally studied by varying the areal loading of the active material (Figure 6b). This test was performed considering the challenge in Li−S batteries that severe insulating characteristics of elemental sulfur degrades the electrochemical performance substantially with increasing areal loading. Notably, reports[10,28,48−50,89−100] on the electrochemical performance of sulfurized polymers with high areal loadings are limited. At 0.2C, S-COP-99(1:4) exhibited initial capacities of 650.6 and 437.9 mAh g^{-1} for areal loadings of 3.0 and 4.1 mg_{sulfur} cm^{-2}, respectively, in comparison to 928.0 mAh g^{-1} for areal loading of 1.0 mg_{sulfur} cm^{-2}. After 150 cycles, the gravimetric capacities of those three electrodes were 724.8, 609.8, and 471.6 mAh g^{-1} with capacity retentions of 78.1%, 93.7%, and 107.7%, respectively. The capacity retention exceeding 100% for 4.1 mg_{sulfur} cm^{-2} loading was possibly due to some kind of activation process of sulfur due to increased electric resistance, although an in-depth investigation is needed to elucidate detailed mechanism.

The effect of covalent attachment of sulfur to the COP-99 framework was studied focusing on the tap density of the electrode. For same sulfur loading of 3.0 mg_{sulfur} cm^{-2}, cross-sectional SEM analyses (SI Figure S7) of both S-COP-99(1:4) and C−S composite control sample were carried out. The S-COP-99(1:4) electrode exhibited a smaller thickness of 57.2 μm than that of the C−S composite electrode (69.4 μm). This result can be explained using high magnification SEM micrographs which showed more compact electrode layer for S-COP-99(1:4) with less cracks and voids. The higher electrode density of S-COP-99(1:4) arose from the covalent attachment of sulfur to the polymer with soft mechanical property. By contrast, physical mixing of sulfur and carbon material in the C−S composite inevitably led to voids and cracks originating from incompatible mechanical properties of both the components as well as less ductile character of carbon materials. The specific capacities, cycling performance, and areal loadings of polymeric sulfur materials reported recently as Li−S battery cathodes are summarized in SI Table S1 for comparison. We expect that the specific capacities for the areal loading of 4.1 mg_{sulfur} cm^{-2} could be increased further by roll-pressing with 1D or 2D carbon conductive agents, but left this task for future industrial optimization.

CONCLUSIONS

Templates that serve for sulfur cathodes in Li−S batteries in conjunction with sulfur impregnation are desired to have two properties: limited pore dimensions for mitigating polysulfides dissolution and high sulfur contents for competitive energy density of the corresponding cells. Unfortunately, these two properties are often mutually exclusive since small pores for preventing polysulfides dissolution sacrifice the energy density due to limited impregnation of sulfur. In the current study, we have overcome this challenge by employing a fluorinated covalent organic polymer, namely COP-99, with well-defined micropores. The aromatic fluorines facilitated S_NAr mechanism to realize sulfur content over 70 wt %, whereas the limited pore dimensions (under 2 nm) along with heteroatoms that have great affinity for LiPSs, effectively slowed down the LiPSs dissolution, resulting in highly sustainable operation of the S-COP-99 cathode. It is of importance that the observed performance arose from an unconventional strategy, one that relies on sulfur as a nucleophile to attack electron-deficient aromatic compounds.

ASSOCIATED CONTENT

Supporting Information

The Supporting Information is available free of charge on the ACS Publications website at DOI: 10.1021/acs.chemmater.9b01986.

Details of NLDFT based on infinite slit pore approximation; additional FT-IR, TGA, XPS, and FE-SEM results of COP-99 and S-COP-99s; additional cycling performance data; and conditions and cell performance of reported organosulfur electrodes (PDF)

AUTHOR INFORMATION

Corresponding Authors

*E-mail: khchar@snu.ac.kr (K.C.).
*E-mail: yavuz@kaist.ac.kr (C.T.Y.).
*E-mail: jangwookchoi@snu.ac.kr (J.W.C.).

ORCID

Kookheon Char: 0000-0002-7938-8022
Cafer T. Yavuz: 0000-0003-0580-3331
Jang Wook Choi: 0000-0001-8783-0901

Author Contributions

§H.S., D.K., and H.J.K. contributed equally.

Notes

The authors declare no competing financial interest.

ACKNOWLEDGMENTS

C.T.Y. acknowledges funding support from the National Research Foundation of Korea (NRF-2017M3A7B4042140). J.W.C. acknowledges financial support from a National Research Foundation of Korea grant (NRF-2018R1A2A1A19023146 and NRF-2018M1A2A2063340). J.W.C also acknowledges the support by Inter-universe Semiconductor Research Center (ISRC) at Seoul National University.

REFERENCES

(1) Larcher, D.; Tarascon, J.-M. Towards greener and more sustainable batteries for electrical energy storage. *Nat. Chem.* **2015**, *7*, 19−29.
(2) Lu, J.; Chen, Z.; Ma, Z.; Pan, F.; Curtiss, L. A.; Amine, K. The role of nanotechnology in the development of battery materials for electric vehicles. *Nat. Nanotechnol.* **2016**, *11*, 1031−1038.
(3) Bruce, P. G.; Freunberger, S. A.; Hardwick, L. J.; Tarascon, J.-M. Li-O_2 and Li-S batteries with high energy storage. *Nat. Mater.* **2012**, *11*, 19−29.
(4) Van Noorden, R. Sulphur back in vogue for batteries. *Nature* **2013**, *498*, 415−416.
(5) Yang, Y.; Zheng, G.; Cui, Y. Nanostructured sulfur cathodes. *Chem. Soc. Rev.* **2013**, *42*, 3018−3032.
(6) Manthiram, A.; Fu, Y.; Chung, S.-H.; Zu, C.; Su, Y.-S. Rechargeable lithium-sulfur batteries. *Chem. Rev.* **2014**, *114*, 11751−11787.
(7) Choi, J. W.; Aurbach, D. Promise and reality of post-lithium-ion batteries with high energy densities. *Nat. Rev. Mater.* **2016**, *1*, 16013.
(8) Ji, X.; Nazar, L. F. Advances in Li-S batteries. *J. Mater. Chem.* **2010**, *20*, 9821−9826.
(9) Lim, J.; Pyun, J.; Char, K. Recent approaches for the direct use of elemental sulfur in the synthesis and processing of advanced materials. *Angew. Chem., Int. Ed.* **2015**, *54*, 3249−3258.
(10) Zhang, Y.; Griebel, J. J.; Dirlam, P. T.; Nguyen, N. A.; Glass, R. S.; Mackay, M. E.; Char, K.; Pyun, J. Inverse vulcanization of

DOI: 10.1021/acs.chemmater.9b01986
Chem. Mater. 2019, 31, 7910−7921

elemental sulfur and styrene for polymeric cathodes in Li-S batteries. *J. Polym. Sci., Part A: Polym. Chem.* **2017**, *55*, 107−116.
(11) Manthiram, A.; Fu, Y.; Su, Y.-S. Challenges and prospects of lithium-sulfur batteries. *Acc. Chem. Res.* **2013**, *46*, 1125−1134.
(12) Bresser, D.; Passerini, S.; Scrosati, B. Recent progress and remaining challenges in sulfur-based lithium secondary batteries-a review. *Chem. Commun.* **2013**, *49*, 10545−10562.
(13) Ji, X.; Lee, K. T.; Nazar, L. F. A highly ordered nanostructured carbon-sulphur cathode for lithium-sulphur batteries. *Nat. Mater.* **2009**, *8*, 500−506.
(14) Li, Z.; Jiang, Y.; Yuan, L.; Yi, Z.; Wu, C.; Liu, Y.; Strasser, P.; Huang, Y. A highly ordered meso@ microporous carbon-supported sulfur@ smaller sulfur core-shell structured cathode for Li-S batteries. *ACS Nano* **2014**, *8*, 9295−9303.
(15) Li, G.; Sun, J.; Hou, W.; Jiang, S.; Huang, Y.; Geng, J. Three-dimensional porous carbon composites containing high sulfur nanoparticle content for high-performance lithium-sulfur batteries. *Nat. Commun.* **2016**, *7*, 10601.
(16) Zu, C.; Manthiram, A. Hydroxylated graphene-sulfur nanocomposites for high-rate lithium-sulfur batteries. *Adv. Energy Mater.* **2013**, *3*, 1008−1012.
(17) Peng, H. J.; Huang, J. Q.; Zhao, M. Q.; Zhang, Q.; Cheng, X. B.; Liu, X. Y.; Qian, W. Z.; Wei, F. Nanoarchitectured graphene/CNT@ porous carbon with extraordinary electrical conductivity and interconnected micro/mesopores for lithium-sulfur batteries. *Adv. Funct. Mater.* **2014**, *24*, 2772−2781.
(18) Cheng, Z.; Xiao, Z.; Pan, H.; Wang, S.; Wang, R. Elastic sandwich-type rGO-VS2/S composites with high tap density: structural and chemical cooperativity enabling lithium-sulfur batteries with high energy density. *Adv. Energy Mater.* **2018**, *8*, 1702337.
(19) Song, M.-K.; Zhang, Y.; Cairns, E. J. A long-life, high-rate lithium/sulfur cell: a multifaceted approach to enhancing cell performance. *Nano Lett.* **2013**, *13*, 5891−5899.
(20) Zhang, K.; Xu, Y.; Lu, Y.; Zhu, Y.; Qian, Y.; Wang, D.; Zhou, J.; Lin, N.; Qian, Y. A graphene oxide-wrapped bipyramidal sulfur@ polyaniline core-shell structure as a cathode for Li-S batteries with enhanced electrochemical performance. *J. Mater. Chem. A* **2016**, *4*, 6404−6410.
(21) Hwa, Y.; Seo, H. K.; Yuk, J.-m.; Cairns, E. J. Freeze-dried sulfur-graphene oxide-carbon nanotube nanocomposite for high sulfur-loading lithium/sulfur cells. *Nano Lett.* **2017**, *17*, 7086−7094.
(22) Sun, Q.; He, B.; Zhang, X.-Q.; Lu, A.-H. Engineering of hollow core-shell interlinked carbon spheres for highly stable lithium-sulfur batteries. *ACS Nano* **2015**, *9*, 8504−8513.
(23) Pei, F.; An, T.; Zang, J.; Zhao, X.; Fang, X.; Zheng, M.; Dong, Q.; Zheng, N. From hollow carbon spheres to N-doped hollow porous carbon bowls: rational design of hollow carbon host for Li-S batteries. *Adv. Energy Mater.* **2016**, *6*, 1502539.
(24) Tang, C.; Zhang, Q.; Zhao, M. Q.; Huang, J. Q.; Cheng, X. B.; Tian, G. L.; Peng, H. J.; Wei, F. Nitrogen-doped aligned carbon nanotube/graphene sandwiches: Facile catalytic growth on bifunctional natural catalysts and their applications as scaffolds for high-rate lithium-sulfur batteries. *Adv. Mater.* **2014**, *26*, 6100−6105.
(25) Zhao, Y.; Wu, W.; Li, J.; Xu, Z.; Guan, L. Encapsulating MWNTs into hollow porous carbon nanotubes: A tube-in-tube carbon nanostructure for high-performance lithium-sulfur batteries. *Adv. Mater.* **2014**, *26*, 5113−5118.
(26) Lin, Z.; Zeng, Z.; Gui, X.; Tang, Z.; Zou, M.; Cao, A. Carbon nanotube sponges, aerogels, and hierarchical composites: Synthesis, properties, and energy applications. *Adv. Energy Mater.* **2016**, *6*, 1600554.
(27) Yang, Y.; Yu, G.; Cha, J. J.; Wu, H.; Vosgueritchian, M.; Yao, Y.; Bao, Z.; Cui, Y. Improving the performance of lithium-sulfur batteries by conductive polymer coating. *ACS Nano* **2011**, *5*, 9187−9193.
(28) Oschmann, B.; Park, J.; Kim, C.; Char, K.; Sung, Y.-E.; Zentel, R. Copolymerization of polythiophene and sulfur to improve the electrochemical performance in lithium-sulfur batteries. *Chem. Mater.* **2015**, *27*, 7011−7017.
(29) Xiao, P.; Bu, F.; Yang, G.; Zhang, Y.; Xu, Y. Integration of graphene, nano sulfur, and conducting polymer into compact, flexible lithium-sulfur battery cathodes with ultrahigh volumetric capacity and superior cycling stability for foldable devices. *Adv. Mater.* **2017**, *29*, 1703324.
(30) Wu, H. B.; Wei, S.; Zhang, L.; Xu, R.; Hng, H. H.; Lou, X. W. Embedding sulfur in MOF-derived microporous carbon polyhedrons for lithium-sulfur Batteries. *Chem. - Eur. J.* **2013**, *19*, 10804−10808.
(31) Zheng, J.; Tian, J.; Wu, D.; Gu, M.; Xu, W.; Wang, C.; Gao, F.; Engelhard, M. H.; Zhang, J.-G.; Liu, J.; Xiao, J. Lewis acid-base interactions between polysulfides and metal organic framework in lithium sulfur batteries. *Nano Lett.* **2014**, *14*, 2345−2352.
(32) Chen, T.; Cheng, B.; Zhu, G.; Chen, R.; Hu, Y.; Ma, L.; Lv, H.; Wang, Y.; Liang, J.; Tie, Z.; Jin, Z.; Liu, J. Highly efficient retention of polysulfides in "sea urchin"-like carbon nanotube/nanopolyhedra superstructures as cathode material for ultralong-life lithium-sulfur batteries. *Nano Lett.* **2017**, *17*, 437−444.
(33) Li, Z.; Li, C.; Ge, X.; Ma, J.; Zhang, Z.; Li, Q.; Wang, C.; Yin, L. Reduced graphene oxide wrapped MOFs-derived cobalt-doped porous carbon polyhedrons as sulfur immobilizers as cathodes for high performance lithium sulfur batteries. *Nano Energy* **2016**, *23*, 15−26.
(34) Tan, Y.; Jia, Z.; Lou, P.; Cui, Z.; Guo, X. Self-assembly sandwiches of reduced graphene oxide layers with zeolitic-imidazolate-frameworks-derived mesoporous carbons as polysulfides reservoirs for lithium-sulfur batteries. *J. Power Sources* **2017**, *341*, 68−74.
(35) Wu, H. B.; Lou, X. W. D. Metal-organic frameworks and their derived materials for electrochemical energy storage and conversion: Promises and challenges. *Sci. Adv.* **2017**, *3*, No. eaap9252.
(36) Yang, X.; Dong, B.; Zhang, H.; Ge, R.; Gao, Y.; Zhang, H. Sulfur impregnated in a mesoporous covalent organic framework for high performance lithium-sulfur batteries. *RSC Adv.* **2015**, *5*, 86137−86143.
(37) Ghazi, Z. A.; Zhu, L.; Wang, H.; Naeem, A.; Khattak, A. M.; Liang, B.; Khan, N. A.; Wei, Z.; Li, L.; Tang, Z. Efficient polysulfide chemisorption in covalent organic frameworks for high-performance lithium-sulfur batteries. *Adv. Energy Mater.* **2016**, *6*, 1601250.
(38) Liao, H.; Wang, H.; Ding, H.; Meng, X.; Xu, H.; Wang, B.; Ai, X.; Wang, C. A 2D porous porphyrin-based covalent organic framework for sulfur storage in lithium-sulfur batteries. *J. Mater. Chem. A* **2016**, *4*, 7416−7421.
(39) Xiao, Z.; Li, L.; Tang, Y.; Cheng, Z.; Pan, H.; Tian, D.; Wang, R. Covalent organic frameworks with lithiophilic and sulfiphilic dual linkages for cooperative affinity to polysulfides in lithium-sulfur batteries. *Energy Storage Materials* **2018**, *12*, 252−259.
(40) Wang, J.; Si, L.; Wei, Q.; Hong, X.; Lin, L.; Li, X.; Chen, J.; Wen, P.; Cai, Y. An imine-linked covalent organic framework as the host material for sulfur loading in lithium-sulfur batteries. *J. Energy Chem.* **2019**, *28*, 54−60.
(41) Guo, B.; Ben, T.; Bi, Z.; Veith, G. M.; Sun, X.-G.; Qiu, S.; Dai, S. Highly dispersed sulfur in a porous aromatic framework as a cathode for lithium-sulfur batteries. *Chem. Commun.* **2013**, *49*, 4905−4907.
(42) Weng, W.; Yuan, S.; Azimi, N.; Jiang, Z.; Liu, Y.; Ren, Y.; Abouimrane, A.; Zhang, Z. Improved cyclability of a lithium-sulfur battery using POP-Sulfur composite materials. *RSC Adv.* **2014**, *4*, 27518−27521.
(43) Talapaneni, S. N.; Hwang, T. H.; Je, S. H.; Buyukcakir, O.; Choi, J. W.; Coskun, A. Elemental-sulfur-mediated facile synthesis of a covalent triazine framework for high-performance lithium-sulfur batteries. *Angew. Chem., Int. Ed.* **2016**, *55*, 3106−3111.
(44) Zhai, W.; Tu, W.; Liu, Y.; Gao, H.; Yu, J.; Zhao, Y.; Li, G. Excellent performance of lithium-sulfur batteries with carbonized porous aromatic framework nanobeads as support. *Electrochim. Acta* **2016**, *219*, 143−151.
(45) Pan, H.; Cheng, Z.; Xiao, Z.; Li, X.; Wang, R. The fusion of imidazolium-based ionic polymer and carbon nanotubes: One type of

DOI: 10.1021/acs.chemmater.9b01986
Chem. Mater. 2019, 31, 7910−7921

new heteroatom-doped carbon precursors for high-performance lithium-sulfur batteries. *Adv. Funct. Mater.* **2017**, *27*, 1703936.
(46) Zeng, J. H.; Wang, Y. F.; Gou, S. Q.; Zhang, L. P.; Chen, Y.; Jiang, J. X.; Shi, F. Sulfur in hyper-cross-linked porous polymer as cathode in lithium-sulfur batteries with enhanced electrochemical properties. *ACS Appl. Mater. Interfaces* **2017**, *9*, 34783−34792.
(47) Zhou, B.; Hu, X.; Zeng, G.; Li, S.; Wen, Z.; Chen, L. Bottom-up construction of porous organic frameworks with built-in TEMPO as a cathode for lithium-sulfur batteries. *ChemSusChem* **2017**, *10*, 2955−2961.
(48) Chung, W. J.; Griebel, J. J.; Kim, E. T.; Yoon, H.; Simmonds, A. G.; Ji, H. J.; Dirlam, P. T.; Glass, R. S.; Wie, J. J.; Nguyen, N. A.; et al. The use of elemental sulfur as an alternative feedstock for polymeric materials. *Nat. Chem.* **2013**, *5*, 518−524.
(49) Kim, H.; Lee, J.; Ahn, H.; Kim, O.; Park, M. J. Synthesis of three-dimensionally interconnected sulfur-rich polymers for cathode materials of high-rate lithium-sulfur batteries. *Nat. Commun.* **2015**, *6*, 7278.
(50) Je, S. H.; Kim, H. J.; Kim, J.; Choi, J. W.; Coskun, A. Perfluoroaryl-elemental sulfur S_NAr chemistry in covalent triazine frameworks with high sulfur contents for lithium-sulfur batteries. *Adv. Funct. Mater.* **2017**, *27*, 1703947.
(51) Wang, D.-G.; Li, N.; Hu, Y.; Wan, S.; Song, M.; Yu, G.; Jin, Y.; Wei, W.; Han, K.; Kuang, G.-C.; Zhang, W. Highly fluoro-substituted covalent organic framework and its application in lithium-sulfur batteries. *ACS Appl. Mater. Interfaces* **2018**, *10*, 42233−42240.
(52) Byun, J.; Patel, H. A.; Thirion, D.; Yavuz, C. T. Charge-specific size-dependent separation of water-soluble organic molecules by fluorinated nanoporous networks. *Nat. Commun.* **2016**, *7*, 13377.
(53) Patel, H. A.; Yavuz, C. T. Noninvasive functionalization of polymers of intrinsic microporosity for enhanced CO_2 capture. *Chem. Commun.* **2012**, *48*, 9989−9991.
(54) Thirion, D.; Kwon, Y.; Rozyyev, V.; Byun, J.; Yavuz, C. T. Synthesis and easy functionalization of highly porous networks through exchangeable fluorines for target specific applications. *Chem. Mater.* **2016**, *28*, 5592−5595.
(55) Tarazona, P.; Marconi, U. M. B.; Evans, R. Phase equilibria of fluid interfaces and confined fluids: non-local versus local density functionals. *Mol. Phys.* **1987**, *60*, 573−595.
(56) Tarazona, P. Free-energy density functional for hard spheres. *Phys. Rev. A: At., Mol., Opt. Phys.* **1985**, *31*, 2672−2679.
(57) Kende, I.; Pickering, T.; Tobolsky, A. The dissociation energy of the tetrasulfide linkage. *J. Am. Chem. Soc.* **1965**, *87*, 5582−5586.
(58) Luo, Y.-R.; Kerr, J. In *CRC Handbook of Chemistry and Physics*; Hayens, W. M., Ed.; CRC Press/Taylor and Francis: Boca Raton, 2012; p 92.
(59) Li, S.; Zhou, Q.; Chu, W.; Zhao, W.; Zheng, J. Surface-enhanced Raman scattering behaviour of 4-mercaptophenyl boronic acid on assembled silver nanoparticles. *Phys. Chem. Chem. Phys.* **2015**, *17*, 17638−17645.
(60) Socrates, G. *Infrared and Raman Characteristic Group Frequencies: Tables and Charts*; John Wiley & Sons: Hoboken, 2004.
(61) Dai, Q.; Xue, C.; Xue, G.; Jiang, L. Fourier-transform surface enhanced Raman scattering studies of molecular self-assembly of disulfides on metals and the application in adhesion promotion. *J. Adhes. Sci. Technol.* **1995**, *9*, 1465−1474.
(62) Xue, G.; Ma, M.; Zhang, J.; Lu, Y.; Carron, K. T. SERS and XPS studies of the molecular orientation of thiophenols from the gaseous state onto silver. *J. Colloid Interface Sci.* **1992**, *150*, 1−6.
(63) Currell, B.; Williams, A. Thermal analysis of elemental sulphur. *Thermochim. Acta* **1974**, *9*, 255−259.
(64) Kim, E. T.; Chung, W. J.; Lim, J.; Johe, P.; Glass, R. S.; Pyun, J.; Char, K. One-pot synthesis of PbS NP/sulfur-oleylamine copolymer nanocomposites via the copolymerization of elemental sulfur with oleylamine. *Polym. Chem.* **2014**, *5*, 3617−3623.
(65) Konarov, A.; Gosselink, D.; Doan, T. N. L.; Zhang, Y.; Zhao, Y.; Chen, P. Simple, scalable, and economical preparation of sulfur-PAN composite cathodes for Li/S batteries. *J. Power Sources* **2014**, *259*, 183−187.
(66) Li, J.; Li, K.; Li, M.; Gosselink, D.; Zhang, Y.; Chen, P. A sulfur-polyacrylonitrile/graphene composite cathode for lithium batteries with excellent cyclability. *J. Power Sources* **2014**, *252*, 107−112.
(67) Wei, S.; Ma, L.; Hendrickson, K. E.; Tu, Z.; Archer, L. A. Metal-sulfur battery cathodes based on PAN-sulfur composites. *J. Am. Chem. Soc.* **2015**, *137*, 12143−12152.
(68) Peng, H.-J.; Huang, J.-Q.; Liu, X.-Y.; Cheng, X.-B.; Xu, W.-T.; Zhao, C.-Z.; Wei, F.; Zhang, Q. Healing high-loading sulfur electrodes with unprecedented long cycling life: spatial heterogeneity control. *J. Am. Chem. Soc.* **2017**, *139*, 8458−8466.
(69) Fan, F. Y.; Carter, W. C.; Chiang, Y. M. Mechanism and kinetics of Li2S precipitation in lithium-sulfur batteries. *Adv. Mater.* **2015**, *27*, 5203−5209.
(70) Pan, H.; Chen, J.; Cao, R.; Murugesan, V.; Rajput, N. N.; Han, K. S.; Persson, K.; Estevez, L.; Engelhard, M. H.; Zhang, J.-G.; et al. Non-encapsulation approach for high-performance Li-S batteries through controlled nucleation and growth. *Nat. Energy* **2017**, *2*, 813−820.
(71) Seh, Z. W.; Sun, Y.; Zhang, Q.; Cui, Y. Designing high-energy lithium-sulfur batteries. *Chem. Soc. Rev.* **2016**, *45*, 5605−5634.
(72) Huggins, R. A. *Advanced Batteries: Materials Science Aspects*; Springer: Berlin, 2009.
(73) Weppner, W.; Huggins, R. A. Determination of the kinetic parameters of mixed-conducting electrodes and application to the system Li_3Sb. *J. Electrochem. Soc.* **1977**, *124*, 1569−1578.
(74) Yamin, H.; Gorenshtein, A.; Penciner, J.; Sternberg, Y.; Peled, E. Lithium sulfur battery oxidation/reduction mechanisms of polysulfides in THF solutions. *J. Electrochem. Soc.* **1988**, *135*, 1045−1048.
(75) Jung, Y.; Kim, S. New approaches to improve cycle life characteristics of lithium-sulfur cells. *Electrochem. Commun.* **2007**, *9*, 249−254.
(76) Guo, L.; Oskam, G.; Radisic, A.; Hoffmann, P. M.; Searson, P. C. Island growth in electrodeposition. *J. Phys. D: Appl. Phys.* **2011**, *44*, 443001.
(77) Zhang, S.; Xu, K.; Jow, T. Electrochemical impedance study on the low temperature of Li-ion batteries. *Electrochim. Acta* **2004**, *49*, 1057−1061.
(78) Kolosnitsyn, V.; Kuzmina, E.; Karaseva, E.; Mochalov, S. A study of the electrochemical processes in lithium-sulphur cells by impedance spectroscopy. *J. Power Sources* **2011**, *196*, 1478−1482.
(79) Zhang, Z.; Kong, L. L.; Liu, S.; Li, G. R.; Gao, X. P. A High-efficiency sulfur/carbon composite based on 3D graphene nanosheet@ carbon nanotube matrix as cathode for lithium-sulfur battery. *Adv. Energy Mater.* **2017**, *7*, 1602543.
(80) Fan, F. Y.; Woodford, W. H.; Li, Z.; Baram, N.; Smith, K. C.; Helal, A.; McKinley, G. H.; Carter, W. C.; Chiang, Y.-M. Polysulfide flow batteries enabled by percolating nanoscale conductor networks. *Nano Lett.* **2014**, *14*, 2210−2218.
(81) Chen, H.; Zou, Q.; Liang, Z.; Liu, H.; Li, Q.; Lu, Y.-C. Sulphur-impregnated flow cathode to enable high-energy-density lithium flow batteries. *Nat. Commun.* **2015**, *6*, 5877.
(82) Deng, Z.; Zhang, Z.; Lai, Y.; Liu, J.; Li, J.; Liu, Y. Electrochemical impedance spectroscopy study of a lithium/sulfur battery: modeling and analysis of capacity fading. *J. Electrochem. Soc.* **2013**, *160*, A553−A558.
(83) Demir-Cakan, R.; Morcrette, M.; Gangulibabu; Gueguen, A.; Dedryvere, R.; Tarascon, J.-M. Li-S batteries: simple approaches for superior performance. *Energy Environ. Sci.* **2012**, *6*, 176−182.
(84) Canas, N. A.; Hirose, K.; Pascucci, B.; Wagner, N.; Friedrich, K. A.; Hiesgen, R. Investigations of lithium-sulfur batteries using electrochemical impedance spectroscopy. *Electrochim. Acta* **2013**, *97*, 42−51.
(85) Zhang, X.-Q.; Sun, Q.; Dong, W.; Li, D.; Lu, A.-H.; Mu, J.-Q.; Li, W.-C. Synthesis of superior carbon nanofibers with large aspect ratio and tunable porosity for electrochemical energy storage. *J. Mater. Chem. A* **2013**, *1*, 9449−9455.
(86) Zanello, P. *Inorganic Electrochemistry: Theory, Practice and Application*; Rotal Society of Chemistry: London, 2003.

DOI: 10.1021/acs.chemmater.9b01986
Chem. Mater. 2019, 31, 7910−7921

(87) Tao, X.; Wang, J.; Liu, C.; Wang, H.; Yao, H.; Zheng, G.; Seh, Z. W.; Cai, Q.; Li, W.; Zhou, G.; et al. Balancing surface adsorption and diffusion of lithium-polysulfides on nonconductive oxides for lithium-sulfur battery design. *Nat. Commun.* **2016**, *7*, 11203.
(88) Chen, M.; Zhao, S.; Jiang, S.; Huang, C.; Wang, X.; Yang, Z.; Xiang, K.; Zhang, Y. Suppressing the polysulfide shuttle effect by heteroatom-doping for high-performance lithium-sulfur batteries. *ACS Sustain. Chem. Eng.* **2018**, *6*, 7545−7557.
(89) Dirlam, P. T.; Simmonds, A. G.; Kleine, T. S.; Nguyen, N. A.; Anderson, L. E.; Klever, A. O.; Florian, A.; Costanzo, P. J.; Theato, P.; Mackay, M. E.; Glass, R. S.; Char, K.; Pyun, J. Inverse vulcanization of elemental sulfur with 1,4-diphenylbutadiyne for cathode materials in Li-S batteries. *RSC Adv.* **2015**, *5*, 24718−24722.
(90) Chang, A.; Wu, Q.; Du, X.; Chen, S.; Shen, J.; Song, Q.; Xie, J.; Wu, W. Immobilization of sulfur in microgels for lithium-sulfur battery. *Chem. Commun.* **2016**, *52*, 4525−4528.
(91) Je, S. H.; Hwang, T. H.; Talapaneni, S. N.; Buyukcakir, O.; Kim, H. J.; Yu, J.-S.; Woo, S.-G.; Jang, M. C.; Son, B. K.; Coskun, A.; Choi, J. W. Rational sulfur cathode design for lithium-sulfur batteries: Sulfur-embedded benzoxazine polymers. *ACS Energy Lett.* **2016**, *1*, 566−572.
(92) Kim, E. T.; Park, J.; Kim, C.; Simmonds, A. G.; Sung, Y.-E.; Pyun, J.; Char, K. Conformal polymeric multilayer coatings on sulfur cathodes via the layer-by-layer deposition for high capacity retention in Li-S Batteries. *ACS Macro Lett.* **2016**, *5*, 471−475.
(93) Li, B.; Li, S.; Xu, J.; Yang, S. A new configured lithiated silicon-sulfur battery built on 3D graphene with superior electrochemical performances. *Energy Environ. Sci.* **2016**, *9*, 2025−2030.
(94) Chang, C.-H.; Manthiram, A. Covalently grafted polysulfur-graphene nanocomposites for ultrahigh sulfur-loading lithium-polysulfur batteries. *ACS Energy Lett.* **2018**, *3*, 72−77.
(95) Liu, J.; Qian, T.; Wang, M.; Liu, X.; Xu, N.; You, Y.; Yan, C. Molecularly imprinted polymer enables high-efficiency recognition and trapping lithium polysulfides for stable lithium sulfur battery. *Nano Lett.* **2017**, *17*, 5064−5070.
(96) Park, J.; Kim, E. T.; Kim, C.; Pyun, J.; Jang, H. S.; Shin, J.; Choi, J. W.; Char, K.; Sung, Y. E. The importance of confined sulfur nanodomains and adjoining electron conductive pathways in subreaction regimes of Li-S batteries. *Adv. Energy Mater.* **2017**, *7*, 1700074.
(97) Zeng, S.; Li, L.; Xie, L.; Zhao, D.; Wang, N.; Chen, S. Conducting polymers crosslinked with sulfur as cathode materials for high-rate, ultralong-life lithium-sulfur batteries. *ChemSusChem* **2017**, *10*, 3378−3386.
(98) Zeng, S.; Li, L.; Zhao, D.; Liu, J.; Niu, W.; Wang, N.; Chen, S. Polymer-capped sulfur copolymers as lithium-sulfur battery cathode: Enhanced performance by combined contributions of physical and chemical confinements. *J. Phys. Chem. C* **2017**, *121*, 2495−2503.
(99) Kang, H.; Kim, H.; Park, M. J. Sulfur-rich polymers with functional linkers for high-capacity and fast-charging lithium-sulfur batteries. *Adv. Energy Mater.* **2018**, *8*, 1802423.
(100) Zeng, S.; Li, L.; Yu, J.; Wang, N.; Chen, S. Highly crosslinked organosulfur copolymer nanosheets with abundant mesopores as cathode materials for efficient lithium-sulfur batteries. *Electrochim. Acta* **2018**, *263*, 53−59.

DOI: 10.1021/acs.chemmater.9b01986
Chem. Mater. 2019, 31, 7910−7921